Indoor Optical Wireless Communication Coverage Optimization Using a SiPM Photoreceiver

Bastien Béchadergue, Thibauld Cazimajou, Fabien Mandorlo, Calmon F.

Indoor Optical Wireless Communication Coverage Optimization Using a SiPM Photoreceiver

Bastien Béchadergue*, Thibauld Cazimajou†, Fabien Mandorlo† and Francis Calmon†
*Laboratoire d'Ingénierie des Systèmes de Versailles
Université Paris-Saclay, UVSQ, 78140 Vélizy-Villacoublay, France
Email: bastien.bechadergue@uvsq.fr
†Institut des Nanotechnologies de Lyon
University of Lyon, 69621 Villeurbanne Cedex, France
Email: thibauld.cazimajou@univ-lyon1.fr, {fabien.mandorlo, francis.calmon}@insa-lyon.fr

***Abstract*—Although optical wireless communication (OWC) is seen as a promising complementary technology to radio frequency systems, its deployment is currently hampered by its limited communication range and the lack of compactness of its transceivers. A partial solution lies in using more sensitive photoreceivers, such as arrays of single photon avalanche diodes (SPAD). Despite their limited bandwidth and non-linearity, such devices have been shown to support Gbps data transmission while providing greatly enhanced sensitivity compared to conventional photodiodes (PD). However, their potential to increase the communication coverage of an indoor OWC system has never been studied. In this paper, a simulation framework for evaluating this metric using a SPAD-based indoor OWC system is thus detailed and implemented. Results show that an array of SPADs in the order of a mm^2 is enough to ensure connectivity over a whole 16 m^2 room, whereas similar performance with a PD requires a sensitive area of several hundreds of mm^2, hence demonstrating the interest of SPADs for coverage as well as compactness optimization in OWC.**

***Index Terms*—single photon avalanche diode (SPAD), optical wireless communications (OWC), LiFi**

I. Introduction

Optical wireless communications (OWC) have lately been proposed to complement radio frequency (RF) wireless technologies to overcome spectrum limitations while ensuring better communication security at high speed. First commercial products are now available on the market for several applications, from long-distance outdoor communications to indoor light fidelity (LiFi) networking [1]. In LiFi, several access points (AP) are installed on the ceiling to ensure continuous communication coverage to any user equipment (UE) in the room. The APs and UEs are then equipped with optical transceivers, usually composed of visible or infrared (IR) light emitting diodes (LED) for emission and PIN photodiodes (PD) or avalanche photodiodes (APD) for reception [2].

Despite their numerous advantages, such as low cost and linear response, such photoreceivers have a limited sensitivity which, coupled with the optical power restrictions imposed on the LED source to meet lighting or photobiological safety standards, strongly limits the communication coverage of current LiFi systems to a few square meters [1]. Arrays of PDs/APDs are, therefore, often used to collect more optical power and thus extend the coverage, but this is at the cost of compactness. However, other solutions exist, among which a promising one is using more sensitive photoreceivers, like single-photon avalanche diodes (SPAD).

A SPAD is an APD biased above its breakdown voltage so that the detection of a photon generates a self-sustained avalanche process eventually quenched and turned into a pulse [3]. The sum of all pulses generated over a time period then gives a count value that is an estimate of the number of detected photons during this period. SPADs are thus well adapted to very low light levels, even though they suffer from several limitations. Their photon detection efficiency (PDE) is indeed limited, so that only a part of the incident photons leads to pulses. Undesired avalanche events may also appear, at a rate quantified by the dark count rate (DCR), because of noise events correlated to carrier generation inside the SPAD in dark conditions. In addition, the quenching of each avalanche event is followed by a dead time during which the SPAD is unable to detect another photon. To mitigate these limitations, arrays of SPADs may be built, as in [4], where SPAD pixels of 2.5 μm pitch and 21.8% PDE at 940 nm are described.

SPAD arrays, also called silicon photomultipliers (SiPM) for specific typologies, have also been the subject of numerous works for OWC applications [5]. It has indeed been shown that despite their non-linear response and their bandwidth constrained by dead time, SPADs are much more sensitive than APDs [6] and can be used for the reception of on-off keying (OOK) binary optical signals, even when using dimmable light sources [7], and up to data rates of several Gbps [8]. More complex modulation schemes like orthogonal frequency division multiplexing (OFDM) [9] could also be used [10], [11]. However, the possible gains in communication coverage that could be achieved through the use of SiPM do not yet seem to have been quantified, which is therefore the main objective of this article.

To do that, we first describe the general architecture of the indoor OWC system studied (Section II-A), and focus then on the OFDM modulation adopted (Section II-B), the OWC channel model (Section II-C) and the working principles of both standard PDs and SiPMs (Section II-D). Then, we detail the MATLAB simulation framework we have built (Section III-A) to explore the influence of the size (Section III-B) and number (Section III-C) of the SPADs constituting the SiPM on the communication coverage, defined here as the

zone where the bit error rate (BER) of the received signal is below a forward error correction (FEC) threshold of 3.8^{-3} [12]. Finally, and before concluding the paper (Section IV), we compare the coverage performance enabled by a SiPM receiver with that enabled by a PD receiver (Section III-D).

The obtained results show, on the one hand, that when considering a SiPM of fixed sensitive area, then the lower the dimensions of the SPADs filling it – and thus the larger their number – the better the coverage. On the other hand, they show that the required sensitive area of a SiPM to ensure connectivity over a 16 m^2 room is only in the order of a mm^2, when that of a PD with similar performance would be of several hundreds of mm^2. Therefore, they confirm the great interest of SiPMs as OWC receivers to optimize coverage and compactness and thus to pave the way for their integration in small UEs like smartphones.

II. System Architecture and Modelling

A. System Architecture and Channel Model

In order to evaluate the interest of SiPM-based receivers for OWC coverage optimization, we have defined and simulated the system represented in Fig. 1. This system is composed, on the infrastructure side, of an AP equipped with a single IR LED and that is mounted on the ceiling of a 4×4×2.5 m indoor room. This AP transmits an optical data signal modulated using DCO-OFDM (see Section II-B). After free space propagation (see Section II-C), this signal is received by the UE, which may move on an x-y plane 0.85 m above the floor, and which is equipped with both a PD receiver and a SiPM receiver (see Section II-D).

From a geometrical point of view, the studied setup is such that the UE is always pointing toward the ceiling, whereas the AP is always oriented toward the floor. In other words, the optical axis of the AP, noted $\overrightarrow{n_{\text{AP}}}$ in Fig. 1, and that of the UE, noted $\overrightarrow{n_{\text{UE}}}$, are such that whatever the position of the UE, $\overrightarrow{n_{\text{UE}}} = -\overrightarrow{n_{\text{AP}}} = [0, 0, 1]$. This also means that the irradiance angle ϕ and the incidence angle ψ are always equal. Although simplistic, this setup is indeed the one proposed by most current LiFi products [13].

B. DCO-OFDM Data Transmission Principles

Before being transmitted as an optical signal, the binary data stream to send is modulated using the well known DCO-OFDM scheme [9], which main steps are detailed on the left part of Fig. 1. First, this binary stream is mapped using a quadrature amplitude modulation (QAM) of order M. The resulting symbols are reshaped from serial-to-parallel (S/P) over $N/2$ branches, with N the number of subcarriers, and where the first branch is set to zero whereas the $N/2-1$ branches left are filled with consecutive M-QAM symbols.

Hermitian symmetry is then applied to the resulting vector, which gives a larger vector of N symbols, noted here $\mathbf{X} = [0, X_1, X_2, \cdots, X_{N-1}]$, and where $X_{N-k} = X_k^*$ for $0 < k < N/2$. This, along with the fact the zeroth and $N/2$-th subcarriers are set to zero, ensures that the output of the inverse fast Fourier transform (IFFT), which comes right after the Hermitian symmetry, produces a time vector $\mathbf{x} = [x_0, x_1, \cdots, x_{N-1}]$ of real numbers.

TABLE I: DCO-OFDM Parameters.

Parameter	Value
Signal bandwidth (B)	5 MHz
Number of sub-carriers (N)	16
Sub-carrier spacing (f_{scs})	312.5 kHz
Symbol duration (T_{symb})	4 μs
Length of the CP (L_{cp})	4
Sampling period (T_s)	200 ns
QAM order of each sub-carrier (M)	16
Data rate (R_b)	16 Mbps

After parallel-to-serial (P/S) conversion, a cyclic prefix (CP) is appended at the beginning of this time vector by adding its L_{cp}-th last samples (i.e. the vector $\left[x_{N-L_{cp}+1}, \cdots, x_N\right]$) to prevent inter-symbol interference (ISI) caused by multipath. The resulting signal is finally converted into an analogue signal by a digital-to-analog converter (DAC), amplified and added to a continuous bias current to meet the electrical constraints of the LED and its driver.

After propagation, the incident optical signal is turned into an electrical signal by either the PD or the SiPM. This signal is digitized by an analog-to-digital converter (ADC) and then processed as follows: the CP is first removed, after which the time-domain symbol $\mathbf{y} = [y_0, y_1, \cdots, y_{N-1}]$ is parallelized to go through an FFT which outputs N M-QAM symbols $\mathbf{Y} = [Y_0, Y_1, \cdots, Y_{N-1}]$ that are finally equalized, serialized and demapped to recover a binary stream.

In practice, as highlighted in Table I, the total DCO-OFDM signal bandwidth B has been chosen to meet the modulation bandwidth of a 5 MHz IR LED [14]. The number of subcarriers has then been set to $N = 16$, with a subcarrier spacing $f_{scs} = 312.5$ kHz, which means the time symbol duration is $T_{symb} = 4$ μs. Each symbol is composed of $N = 16$ time samples plus a CP of length $L_{cp} = 4$, so that the sampling period is $T_s = 200$ ns. Finally, each subcarrier is modulated using a QAM scheme of order $M = 16$, so that the total data rate is $R_b = N \log_2(M)/T_{symb} = 16$ Mbps. Higher data rates could be achieved using a larger modulation bandwidth and QAM order, but this would increase the duration of the simulation and is not our focus, hence this low data rate.

C. Channel Model

In order to estimate the communication coverage of our system, we first need to simulate the continuous current signal $i(t)$ and the discrete count signal N_k produced respectively by the PD and the SiPM in the UE from the optical signal sent by the AP. In both cases, these output signals will depend on the instantaneous optical power $\Phi_r(t)$ incident to the receiver sensitive area, which depends itself on the instantaneous optical power $\Phi_t(t)$ transmitted by the source and on the channel impulse response (CIR).

The CIR is, in practice, composed of a line-of-sight (LoS) component coming from the direct propagation path of length d between the AP and the UE, along with non-LoS (NLoS) components coming from reflections on the walls and obstacles. However, these NLoS paths are neglected here as their contribution can be considered negligible, except at the room's edges [15]. In addition, we assume the channel remains relatively flat up to a few tens of MHz, so that the CIR can

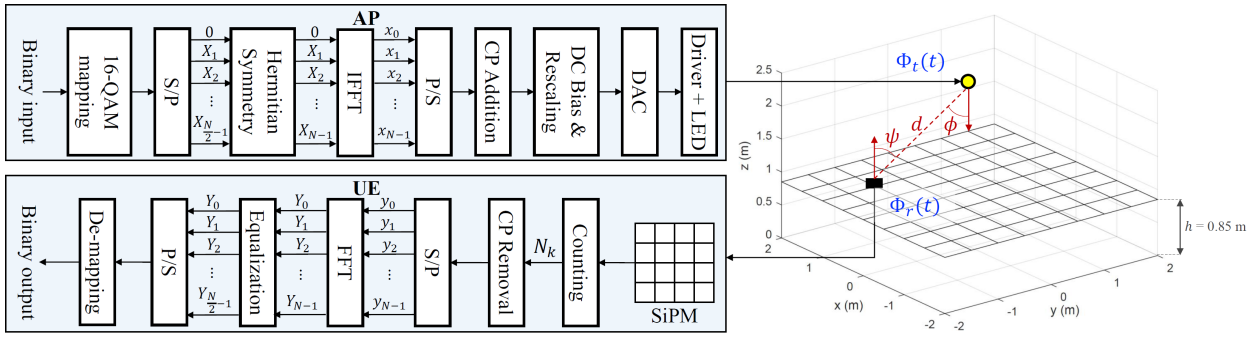

Fig. 1: Block diagram of the system studied, in the case of a SiPM receiver, and illustration of the link geometry.

be modeled as a simple channel DC gain $H_{\text{LoS}}(0)$. In such a case, the instantaneous incident optical power $\Phi_r(t)$ and the instantaneous transmitted optical power $\Phi_t(t)$ are such that $\Phi_r(t) = H_{\text{LoS}}(0)\Phi_t(t)$, with [2]:

$$H_{\text{LoS}}(0) = \begin{cases} \frac{A_r(m+1)}{2\pi d^2}\cos^m(\phi)\cos(\psi) \\ \text{if } 0 \leq \phi \leq \pi/2 \text{ and } 0 \leq \psi \leq \psi_c, \\ 0 \text{ otherwise,} \end{cases} \quad (1)$$

where A_r is the sensitive area of the photoreceiver, and m is the order of Lambertian emission of the LED source that models its directivity and depends on its semi-angle at half power $\Phi_{1/2}$ according to $m = -\ln 2/\ln\left(\cos\left(\Phi_{1/2}\right)\right)$. Note in addition that according to (1), the transmitted signal can only be collected by the photoreceiver if its angle of incidence ψ is smaller than the field of view (FoV) ψ_c of the UE.

D. PD and SiPM-Based Photoreceiver Modeling

The way the incident optical signal is turned into an exploitable output signal depends on the type of photoreceiver. In the case of the PD, the output signal is a photocurrent that can be converted into a voltage signal using a transimpedance amplifier (TIA) and which can then be digitized and processed to recover the transmitted data. In such a case, the output photocurrent $i(t)$ can be approximated as:

$$i(t) = R_{\text{PD}}\Phi_t(t)H_{\text{LoS}}(0) + n(t), \quad (2)$$

with R_{PD} the PD responsivity and $n(t)$ the white Gaussian noise added by the PD, of power spectral density (PSD) N_0.

In the case of a SiPM receiver, the output signal is not a current but a discrete count value. A SiPM is an array of microcells that each contains a SPAD, i.e. an APD biased above its breakdown voltage and connected to a quenching mechanism that can be purely passive or active [3]. When a photon is absorbed by a SPAD, an electron-hole pair may be generated leading to a self-sustained avalanche process due to carrier multiplication. This will increase the current flowing through the passive or active quenching circuitry, which will in turn decrease the reverse bias voltage to eventually quench the avalanche process. Then, the SPAD will need to be recharged to be biased back above its breakdown voltage and thus be able to detect another photon. During this recovery process, called dead time, the SPAD is insensitive to light [11]. Another important feature of SPAD is the PDE, that is the ratio between the detected events (subtracting the noise events to consider only the events correlated to photons) divided by the total number of incident photons. As mentioned in Section I, noise-related avalanche events may also occur, as quantified by the DCR. In any case, once avalanche events occur, they can be easily detected and converted to fast digital pulses.

In order to multiply the number of detected photons, SPADs are often arranged in arrays, as described in [4]. The advantage of using a SPAD array is that the incident photons are spread across the different SPADs, so that at any time, the probability of detecting a photon is higher. Digital SiPMs are a specific type of SPAD arrays, where each detected photon will actually generate a digital pulse, so that a simple sum of all pulses generated by the SPADs during a given time interval $[kT_s, (k+1)T_s]$ of duration T_s will eventually give a count number N_k that is an approximate image of the average incident optical power $\Phi_{r,k}$ over this interval.

Given the random nature of the photon arrival process and because of the SPADs dead time, SiPMs have a non-linear response and there is no exact closed-form expression linking N_k and $\Phi_{r,k}$. However, it can first be show that the maximum count value $N_{k,max}$ of each SPAD is actually independent from $\Phi_{r,k}$, and is only linked with the exposure duration T_s and the dead time T_{dead} according to [6]:

$$N_{k,max} = \frac{T_s}{T_{dead}}. \quad (3)$$

In addition, a simple method proposed in [11] and relying on Monte Carlo simulations can be used to estimate N_k as a function of $\Phi_{r,k}$. It consists in assuming the time interval Δt_p between the arrival of two adjacent photons follows an exponential distribution. Then, such time intervals can be simulated using the inverse cumulative distribution function method, according to which:

$$\Delta t_p = -\frac{E_p}{\eta\Phi_{r,k}}\ln(1-u), \quad (4)$$

where u is a uniformly distributed random variable within 0 and 1, and $E_p = \frac{hc}{\lambda}$ is the energy of a photon of wavelength λ, with h the Planck constant and c the speed of light. As detailed in Table II of [11], this approach can then be used in a loop to simulate the arrival of several consecutive photons on a duration T_s and to extract the count value produced by the SPAD while taking into account the dead time T_{dead}. This is eventually the method we adopted in the present work.

TABLE II: SIMULATION PARAMETERS.

APs parameters	
Parameter	**Value**
[x,y,z] coordinates of the AP	[0,0,0]
Wavelength of operation (λ)	940 nm
Semi-angle at half-power ($\Phi_{1/2}$)	60°
Average optical power radiated (Φ_t)	1.45 W [14]
Number of bits sent	28,000

UE parameters	
Parameter	**Value**
Height of the UE	0.85 m (i.e. h = 1.65 m)
FOV of the photoreceiver (ψ_c)	85° [16]
Responsivity of the PD (R_{PD})	0.63 A/W [16]
Effective area of the PD (A_{PD})	26.4 mm^2 [16]
Noise PSD (N_0)	10^{-21} W/Hz [17]
Side length of the SPADs (p and q)	5, 12.5, 25, 37.5 and 50 μm
Number of SPADs (N_{SPAD})	Variable
PDE of the SPADs (η)	0.2
Dead time of the SPADs (T_{dead})	5 ns

Note that (3) highlights the problems that may arise when the dead time is longer than the exposure duration, in which case the number of counts may be null and ISI is observed [11]. In this work, we assume the counting period of the SiPM is synchronized with the sampling period of the data signal. This means that each count value N_k is obtained after the reception, for a duration $T_s = 200$ ns, of the constant optical power $\Phi_{r,k}$. In addition, we assume a dead time $T_{dead} = 5$ ns, so that there is no ISI and $N_{k,max} = 40$. Note also that other fundamental phenomena of SPAD such as dark counts are neglected here. Typical DCR values are indeed in the order of 1000 counts per second, but the transmitted signal has only a duration of about 4 ms. The probability of appearance of a dark count is therefore low enough to be neglected.

III. SIMULATIONS AND DISCUSSION

A. Simulation Objectives and Parameters

The objective of the simulations that have been carried out is to understand the influence of the size and number of SPADs composing the SiPM receiver on the communication coverage of the system, and to compare this coverage performance with that obtained using a reference PD-based photoreceiver. For this purpose, we consider as a simulation environment the indoor room of 4×4×2.5 m described in Section II-A. The IR LED-based AP is placed at the center of the ceiling and is oriented toward the floor, whereas the UE can move to any point of a x-y receiver plane placed 85 cm above the floor and is oriented toward the ceiling. The coverage performance is then determined by evaluating with MATLAB at which points of the receiver plane the BER, calculated from the transmission of 28,000 bits, is lower than a FEC threshold of 3.8×10^{-3} [12].

The parameters of the DCO-OFDM signals transmitted in these simulations are listed with their values in Table I whereas those of the AP and UE are listed in Table II. On the AP side, it may be noted that the IR LED source operates at a center wavelength of 940 nm and emits an average optical power of 1.45 W with a semi-angle at half power of 60°. On the UE side, it may be noted that the PD-based photoreceiver is actually composed of a Hamamatsu S6967 PD, from the datasheet of which the values for the FOV ψ_c, the responsivity R_{PD} and the sensitive area A_{PD} are taken [16]. In addition, the PSD N_0 of the noise at the PDs level is set to 10^{-21} W/Hz following the literature [17].

This PD-based photoreceiver will serve in Section III-D as a reference to compare the coverage performance with that of the SiPM-based receiver. In between, the influence of the SiPM geometry will be studied by varying parameters related to its size A_{SiPM}, like the SPADs dimensions p and q and their number N_{SPAD}. As noted in Section II-D, the DCR is not taken into account as its influence on the count value over a reading period as short as 200 ns is negligible. Afterpulsing is also not taken into account but left for future works.

B. Influence of the SPAD Size

First, we studied the influence of the size of the SPADs constituting the SiPM on the communication coverage. We considered five different SiPM, each composed of $N_{SPAD} = 100$ SPADs of respective sides $p = q = 5$ μm, 12.5 μm, 25 μm, 37.5 μm and 50 μm, i.e. of respective sensitive area 0.0025 mm^2, 0.0156 mm^2, 0.0625 mm^2, 0.1406 mm^2 and 0.25 mm^2. For each SiPM, we calculated the BER of the data signal received by the UE placed on the optical axis of the AP and facing it (i.e. $\phi = \psi = 0$), and moving from 20 cm to 5 m by steps of 10 cm.

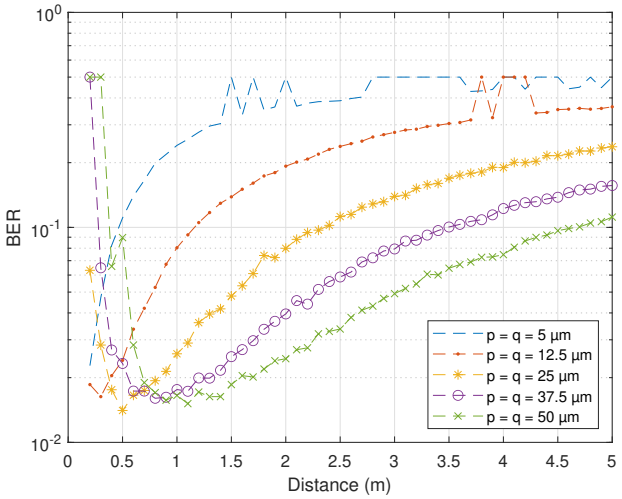

Fig. 2: Evolution of the BER with the distance while the UE faces the AP on its optical axis, and while using SiPMs composed each of 100 SPADs of different size.

Figure 2 shows the resulting BER curves. We can observe that for the SiPMs composed only of SPADs of side 5 μm or 12.5 μm, the BER rises with the distance. This is because as the UE moves away from the AP, the number of incident photons decreases, as does the number of counts produced by the SiPM. The received optical signal is thus converted into a discrete count signal which has less and less different states, which results in a decreasing quantization resolution and eventually leads to an increase in the BER. The variation in the number of counts is sometimes even so small that the signal becomes impossible to demodulate, hence the BER peaks up to 0.5 observed in these two curves.

Although the curves for the other SiPMs have the same overall shape as the distance gets larger, we can notice that at a short distance, they tend to reach a local maximum, and even a global maximum of 0.5 when the SPADs side is 37.5 μm or 50 μm. This is because at such distances, the incident photons flux is actually so high that the SPADs saturate and thus produce count values close to the maximum defined in (3). The resulting count signal has thus low variations, which leads to very high BER values. Increasing the distance then reduces the incident photons flux, up to a point where the SPADs do not saturate anymore and reach an optimal working point corresponding to a minimum BER.

C. Influence of the Number of SPADs

The previous results could lead to the conclusion that the larger the SPADs composing the SiPM, the better in terms of BER at a large distance. However, these results were obtained while considering a constant number of SPADs in each SiPM, i.e. SiPMs of different sensitive area. In addition, the BER obtained was nowhere close to the FEC threshold of 3.8×10^{-3}, suggesting these sensitive areas were too small.

Therefore, we now consider again five different types of SPADs ($p = q = 5$ μm, 12.5 μm, 25 μm, 37.5 μm and 50 μm) but that are this time assembled to build five different types of SiPM, having each a total sensitive area equal to either 0.0025 mm^2, 0.125 mm^2, 0.25 mm^2, 0.4735 mm^2 or 0.625 mm^2. For example, 25,000 SPADs of side 5 μm are necessary to build a SiPM of sensitive area 0.625 mm^2, whereas only 250 SPADs of side 50 μm are needed to build an equivalent SiPM. For each of the 25 resulting SiPMs, we considered the setup defined in Section II-A and calculated the BER of the data signal received by the UE as it moves along the diagonal of the room in 10 cm steps.

Figure 3(a) shows the results obtained with the five possible SiPMs composed of 5 μm SPADs, along with the FEC limit to highlight the maximum communication distance in each case. We can first observe again that the BER increases as the UE moves away from the AP, whatever the total sensitive area of the SiPM. As explained previously, this is because of the reduction of the incident optical power with the AP-to-UE distance. At the same time, we can observe that increasing the number of SPADs composing the SiPM, i.e. increasing its total sensitive area A_{SiPM}, helps reduce the BER and thus extends the maximum communication distance.

Although not shown here, the same tendencies have been observed for the SiPMs composed of SPADs of side 12.5 μm, 25 μm, 37.5 μm and 50 μm. In order to compare their respective interest for coverage optimization, Fig. 3(b) therefore shows the evolution of the BER with the five SiPMs of sensitive area $A_{\text{SiPM}} = 0.625$ mm^2 and respectively composed only of SPADs of either 5, 12.5, 25, 37.5 or 50 μm side. We can see that the best coverage is actually obtained with the SiPM composed of 25,000 SPADs of 5 μm side. SiPMs with larger SPADs not only have a shorter maximum communication distance, but also do not achieve as low a BER within the coverage area. This is because the variance of the count signal, and therefore the signal-to-noise ratio, increases faster with the number of SPADs than with their size.

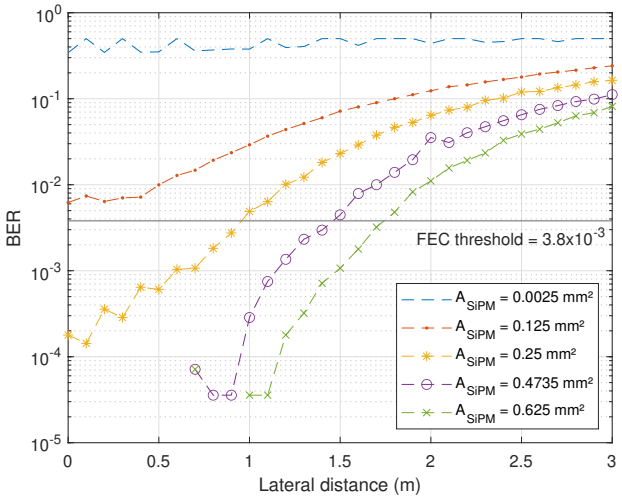

(a) Case of SiPMs of different sensitive areas but all built with 5 μm SPADs.

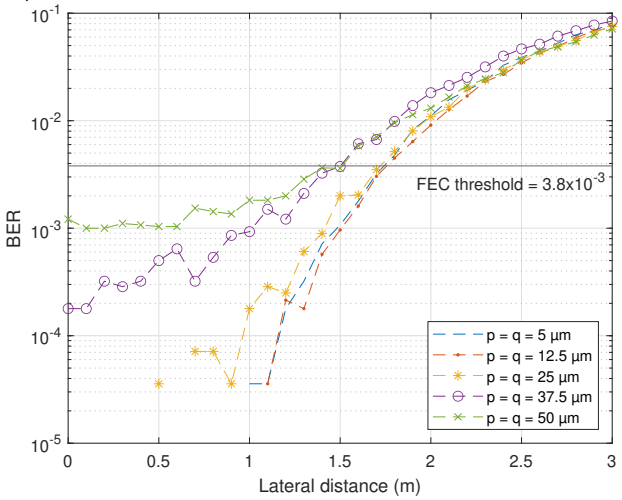

(b) Case of SiPMs of 0.625 mm^2 sensitive area but composed each of SPADs of different size.

Fig. 3: Evolution of the BER along the x axis of the reception place for different types of SiPM.

D. Coverage Performance Comparison

Motivated by the previous conclusions, we defined the SiPM of area $A_{\text{SiPM}} = 0.625$ mm^2 and composed of 25,000 SPADs of 5 μm side as our reference SiPM. Then, we compared the communication coverage it provides with that enabled by the reference PD-based photoreceiver of sensitive area $A_{\text{PD}} = 26.4$ mm^2 defined in Section III-A. We also included in the comparison other SiPM and PD-based photoreceivers, which sensitive area are integer multiples of these reference areas. To do that, we calculated in each case the spatial distribution of the BER along the x-y reception plane defined in Section II-A, by moving the UE along the x and y directions by steps of 10 cm.

Figure 4 shows a top view of the room along with the boundaries of the coverage areas provided by each of these receivers and the share they represent compared to the total area of the room (i.e. 16 m^2). The case of an UE using a single reference PD does not appear because the coverage is actually

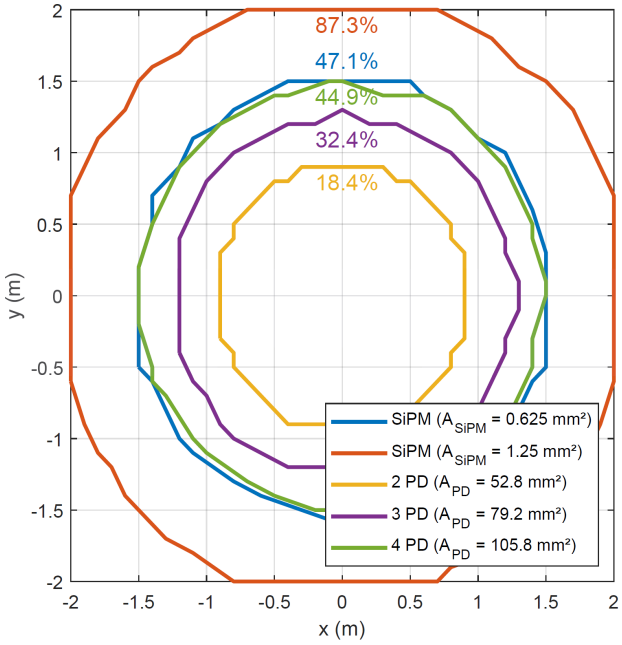

Fig. 4: Top view of the coverage areas ensured by various kinds of SiPMs and arrays of PDs.

null in this case. At least two such PDs are necessary to get connectivity, in which case only 18.4% of the room is covered. The reference SiPM enables on its side to cover 47.1% of the room, a share similar to that obtained with four reference PDs, that is with a PD-based receiver which sensitive area is more than 150 times larger. This share can even be brought up to 87.3% by doubling the SiPM sensitive area, hence showing the great interest of SiPM to extend the coverage performance of an indoor OWC system while maintaining a high compactness level and decent data rate performance.

IV. Conclusions and Future Works

This paper studies on the one hand the influence of the number and size of the SPADs constituting a SiPM receiver on communication coverage of an OWC system, and compares on the other hand this coverage with that obtained using a PD receiver. For this purpose, a simple MATLAB simulation environment is considered, including an IR LED source installed on the ceiling of a $4\times4\times2.5$ m room and a SiPM/PD receiver moving in a plane 85 cm above the floor.

It shows that for a fixed number of SPADs, the larger their dimensions, the better the coverage. However, when considering a SiPM of fixed sensitive area, then the lower the dimensions of the SPADs filling it – and thus the larger their number– the better the coverage. This led us to define a reference SiPM-based OWC receiver, which after comparison with a reference PD receiver (based on the widely used Hamamatsu S6967 PD), exhibits much better coverage performance. For example, in the tested scenario, a BER lower than 3.8×10^{-3} at a data rate of 16 Mbps is reached over around 45% of the room using only a 0.625 mm^2 SiPM, whereas similar performance requires four PDs of total sensitive area 105.8 mm^2. This coverage can even be extended to almost all the room by simply doubling the SiPM sensitive area.

SiPMs therefore have great potential to extend the communication coverage of OWC systems while significantly improving the compactness of the receiver, which is one of the bottlenecks for their integration in small UEs like smartphones. At the same time, they require less incident optical power to provide similar coverage as PDs, which means energy savings could be achieved on the transmitter side. Such conclusions remain, however, to be confirmed in future works, which will include a finer SiPM modeling in the simulations to take into account afterpulsing, dark counts and ambient light, but also experimental demonstrations to evaluate actual BER performance as well as the complexity in using SiPMs in practice.

Acknowledgment

This work was supported by the French National Research Agency (ANR) through the projects SAFELiFi under grant ANR-21-CE25-0001-01 and SPAD-FDSOI under grant ANR-18-CE24-0010.

References

[1] H. Haas *et al.*, "What is LiFi?," *J. Lightw. Technol.*, vol. 34, no. 6, pp. 1533-1544, March 2016.
[2] Z. Ghassemlooy *et al.*, Eds., *Visible Light Communications: Theory and Applications*. Boca Raton, FL, USA: CRC press, 2017.
[3] E. Charbon *et al.* "SPAD-Based Sensors" in *TOF Range-Imaging Cameras*, F. Remondino, and D. Stoppa, Eds., New-York, NY, USA: Springer, 2013, ch. 2, pp. 11–38.
[4] S. Shimada *et al.* "A SPAD Depth Sensor Robust Against Ambient Light: The Importance of Pixel Scaling and Demonstration of a 2.5µm Pixel with 21.8% PDE at 940nm" in *68th IEEE Int. Electron Devices Meeting (IEDM)*, 2022.
[5] E. Fisher, I. Underwood, and R. Henderson, "A Reconfigurable Single-Photon-Counting Integrating Receiver for Optical Communications," *IEEE J. Solid-State Circuits*, vol. 48, no. 7, pp. 1638-1650, July 2013.
[6] L. Zhang *et al.*, "A Comparison of APD- and SPAD-Based Receivers for Visible Light Communications," *J. Lightw. Technol.*, vol. 36, no. 12, pp. 2435-2442, June 2018.
[7] M. Hijazi, S. Huang, and M. Safari, "Adaptive SPAD-based Receiver for Dimmable Visible Light Communication," in *IEEE Wireless Communications and Networking Conf. (WCNC)*, 2022, pp. 2685-2690.
[8] W. Matthews *et al.*, "A 3.45 Gigabits/s SiPM-Based OOK VLC Receiver," *IEEE Photon. Technol. Lett.*, vol. 33, no. 10, pp. 487-490, May 2021.
[9] J. Armstrong, "OFDM for Optical Communications," *J. Lightw. Technol.*, vol. 27, no. 3, pp. 189-204, Feb. 2009.
[10] Y. Li *et al.*, "Optical OFDM With Single-Photon Avalanche Diode," *IEEE Photon. Technol. Lett.*, vol. 27, no. 9, pp. 943-946, May 2015.
[11] C. He, Z. Ahmed, and S. Collins, "Optical OFDM and SiPM Receivers," in *2020 IEEE Globecom Workshops*, 2020, pp. 1-6.
[12] *Forward Error Correction for High Bit-Rate DWDM Submarine Systems*, Recommendations ITU-T G.975.1, International Telecommunication Union, Geneva, Switzerland, Feb. 2004.
[13] B. Béchadergue and B. Azoulay, "An Industrial View on LiFi Challenges and Future," in *12th Int. Symp. on Communication Systems, Networks and Digital Signal Processing (CSNDSP)*, 2020, pp. 1-6.
[14] *DS191 LUXEON IR Domed Line Product Datasheet*, Lumileds Holding B.V., Haarlemmermeer, The Netherlands, 2022.
[15] L. An *et al.*, "Energy Efficiency Optimization for MIMO Visible Light Communication Systems," *IEEE Wireless Commun. Lett.*, vol. 9, no. 4, pp. 452–456, Apr. 2020.
[16] *Si PIN Photodiodes S2506/S6775/S6967 Series*, Hamamatsu, Bridgewater, NJ, USA, 2021.
[17] Y. Hei *et al.*, "Energy-Spectral Efficiency Tradeoff in DCO-OFDM Visible Light Communication System," *IEEE Trans. Veh. Technol.*, vol. 68, no. 10, pp. 9872–9882, Oct. 2019.